How to cite: Angew. Chem. Int. Ed. 2023, e202312130
doi.org/10.1002/anie.202312130

Perovskite Phases Hot Paper

Switching Lead for Tin in $PbHfO_3$: Noncubic Structure of $SnHfO_3$**

*Eric A. Gabilondo, Ryan J. Newell, Rachel Broughton, Aylin Koldemir, Rainer Pöttgen, Jacob L. Jones, and Paul A. Maggard**

Abstract: The removal of lead from commercialized perovskite-oxide-based piezoceramics has been a recent major topic in materials research owing to legislation in many countries. In this regard, Sn(II)-perovskite oxides have garnered keen interest due to their predicted large spontaneous electric polarizations and isoelectronic nature for substitution of Pb(II) cations. However, they have not been considered synthesizable owing to their high metastability. Herein, the perovskite lead hafnate, i.e., $PbHfO_3$ in space group *Pbam*, is shown to react with SnClF at a low temperature of 300 °C, and resulting in the first complete Sn(II)-for-Pb(II) substitution, i.e. $SnHfO_3$. During this topotactic transformation, a high purity and crystallinity is conserved with *Pbam* symmetry, as confirmed by X-ray and electron diffraction, elemental analysis, and ^{119}Sn Mössbauer spectroscopy. In situ diffraction shows $SnHfO_3$ also possesses reversible phase transformations and is potentially polar between ≈130–200 °C. This so-called 'de-leadification' is thus shown to represent a highly useful strategy to fully remove lead from perovskite-oxide-based piezoceramics and opening the door to new explorations of polar and antipolar Sn(II)-oxide materials.

[*] E. A. Gabilondo, P. A. Maggard
Department of Chemistry, North Carolina State University
Raleigh, NC 27695-8204 (USA)
E-mail: Paul_Maggard@ncsu.edu
R. J. Newell, R. Broughton, J. L. Jones
Department of Materials Science and Engineering, North Carolina State University
Raleigh, NC 27695-8204 (USA)
A. Koldemir, R. Pöttgen
Institut für Anorganische und Analytische Chemie, Universität Münster
Corrensstrasse 30, 48149 Münster (Germany)

[**] A previous version of this manuscript has been deposited on a preprint server (https://doi.org/10.26434/chemrxiv-2023-ct3jj).

© 2023 The Authors. Angewandte Chemie International Edition published by Wiley-VCH GmbH. This is an open access article under the terms of the Creative Commons Attribution Non-Commercial NoDerivs License, which permits use and distribution in any medium, provided the original work is properly cited, the use is non-commercial and no modifications or adaptations are made.

Introduction

Technological innovation of electronics requires continual advances in new and complex material fabrication. Thermodynamically stable metal oxides, e.g., SnO_2 or TiO_2, are often used for such applications owing to their high thermal and chemical stability but can be limited by properties such as their large optical band gaps or recombination rates.[1] Recent reports have both predicted[2,3] and shown[4–6] that metastable compounds may have exceptional properties, but a synthesis route is often absent.[7,8] This has given rise to a new frontier of chemistry dedicated to the synthesis and characterization of metastable oxides with a focus on drawing structural connections to predicted new properties. Therefore, development of chemical stabilization techniques and soft-synthesis routes are essential to the preparation of metastable phases,[9] such as low melting molten-fluxes,[10] hydrothermal,[11] and ion-exchange methods.[12] The metathesis techniques use the formidable combination of low reaction temperatures and high ion-diffusion rates to finesse chemical kinetic stabilization lacking in traditional solid-state methodology.[13]

Recent international regulations have mandated the removal of lead from commercial products, and thus, the removal and replacement of lead from perovskite-oxide piezoceramics represents a well-known and critical case in which such emerging techniques can be applied.[14] The targeted structural motif is an A-site cation containing a symmetry-breaking ns^2 electronic configuration (e.g., Pb(II), Sn(II), or Sb(III)) as the postulated origin of large piezo- and ferroelectric polarizations, such as in the commercialized lead zirconate-titanate ($Pb(Zr,Ti)O_3$, or PZT), or antiferroelectricity in the lead zirconates ($PbZrO_3$, or PZO) or hafnates ($PbHfO_3$, or PHO).[15,16] Sn(II)-perovskites are isovalent analogues and are predicted to have even larger polarizations,[17,18] but the synthetic challenges, their high thermodynamic instability, and low thermal stability all inhibit their realization.[19] For example, SnO as a conventional reagent will rapidly oxidize or disproportionate from as low as 250–300 °C, even under inert atmospheres.[20] Despite these obstacles, recent progress has been made by utilizing low-melting Sn(II)-halide salts (e.g., $SnCl_2$) to facilitate efficient cation-exchange in stable precursor structures, such as Ba_2TiO_4 or $K_2Ti_2O_5$ to form 1D, Pb_3O_4-type Sn_2TiO_4,[21,22] and the 2D, ilmenite-type $SnTiO_3$.[23]

In close-packed structures like the cubic perovskite oxides $Ba(Zr,Ti)O_3$ (BZT) and $BaHfO_3$, cation-exchange is more challenging as the rates of ion diffusion are extremely small, i.e., $< 10^{-19}$ $m^2 s^{-1}$. Further, the calculated metastability

 © 2023 The Authors. Angewandte Chemie International Edition published by Wiley-VCH GmbH

of the Sn(II)-substituted perovskites with respect to simpler oxides (e.g., SnO, TiO_2, and ilmenite-$SnTiO_3$) increases dramatically to ≥ 500 meV atom^{-1}.[24,25] In the cubic $BaZrO_3$ or $BaHfO_3$ perovskites, however, the high lattice energy from the rigid MO_6 substructure is sufficiently large to prevent local phase segregation and thus provides additional kinetic stabilization of the Sn(II)-containing perovskite. The structural instability was shown where as much as ≈60–70 % Sn(II)-exchange for Ba(II) in $BaHfO_3$ retains the cubic crystal structure, but ≈30–40 % Sn(II) in BZT can cause the onset of phase segregation. Additionally, in the layered $(Ba_{1-x}Sn_x)_5Nb_4O_{15}$ perovskite, phase segregation into the more stable $SnNb_2O_6$ became prominent at ≈50 % Sn(II)-exchange.[26] Segregation is proposed to occur more readily since the interlayer-Sn(II) ions can more freely diffuse to an energetically favorable coordination environment, although the hypothetical $Sn_5Nb_4O_{15}$ phase is not expected to be nearly as metastable as perovskite-type $SnTiO_3$. The synthesis of Sn(Zr,Ti)O_3 shells on the surfaces of BZT particles (BSZT) demonstrated that cation-exchange and kinetic stabilization of Sn(II) is feasible in the 3D perovskite-type structure, and providing the first evidence that these thus-far only theorized phases do indeed have intriguing properties such as visible-light driven water oxidation.[27] Further developments of these synthetic techniques have led to the first-reported successful synthesis of a fully Sn(II)-substituted perovskite oxide, $SnHfO_3$, stabilized as nano-eggshells.[28]

These observations demonstrate the effectiveness of topotactic ion-exchange in metastable oxide synthesis, and suggesting at least two criteria for the successful synthesis of a desired phase; (I) the underlying substructure must have a strong cohesive energy, and (II) an absence of lower energy polymorphs easily accessible via ion-diffusion. Ion-exchange of Sn(II) in close-packed structures appears to occur topotactically and all (Ba,Sn)MO_3 phases reported thus far are cubic or pseudocubic owing to random displacements of Sn(II) on the A-site. The highest degree of Sn(II)-substitution occurred in phases with high cohesive energies (e.g., M = Zr(IV), Hf(IV)) and had the fewest number of competing polymorphs (e.g., $SnTiO_3$ and $SnNb_2O_6$) regardless of the predicted relative stability. Thus, in order to synthesize a Sn(II)-perovskite with an asymmetric A-site, a precursor with a pre-existing structural distortion away from cubic and with a high cohesive energy might be used in conjunction with '*Chimie Douce*' techniques.[9] In the present work, this approach was explored by combining a low temperature molten-flux exchange reaction with an orthorhombic perovskite oxide having a relatively high cohesive energy, i.e., $PbHfO_3$. The exchange reaction results in full substitution of Pb(II) for Sn(II) on a distorted A-site and the formation of high-purity and polycrystalline $SnHfO_3$ as an orthorhombic perovskite. This marks the first crystalline and fully substituted Sn(II)-perovskite oxide under such conditions and suggests the possibility of lead removal from existing high-performance dielectric materials. The so-called 'de-leadification', or removal of Pb(II), represents a promising direction in the exploratory synthesis of new lead-free dielectrics.

Results and Discussion

The first reported $SnHfO_3$, synthesized from cubic $BaHfO_3$, appeared to be pseudo-cubic according to X-ray diffraction (XRD), likely due to random distortions of Sn(II)-cations on the A-site and no apparent distortion of the HfO_6 polyhedra.[28] The orthorhombic $PbHfO_3$ (PHO) is used herein as an alternative precursor to provide a pre-distorted ordering to the A-site prior to Sn(II)-exchange, while maintaining the high lattice cohesive energy of the HfO_6 substructure. The PHO precursor was first synthesized by a high temperature flux-mediated reaction from binary oxides. The as-synthesized PHO was then reacted with a low-melting SnClF flux (m.p. ≈220–240 °C) at 300 °C according to equation 1:

$$PbHfO_3 + SnClF \rightarrow SnHfO_3 + PbClF \quad (1)$$

The proposed reaction is driven forward by the larger heat of formation of the PbClF product versus the SnClF reactant (≈−35 kJ/mol), detailed in Figure 1. Depicted in Figure 1A, the net reaction is calculated to be exothermic (≈−14 kJ/mol) which allows for the formation of the metastable orthorhombic $SnHfO_3$ product (o-SHO). The activation energy barrier for its formation must be relatively low given the reaction temperature. It is also smaller than the activation energy of decomposition, i.e., $SnHfO_3 \rightarrow SnO + HfO_2$. XRD data of the reaction mixture before and after annealing (Figure S1) confirms the maintenance of the orthorhombic perovskite structure, the removal of SnClF, and crystallization of the PbClF side product. Orthorhombic $SnHfO_3$ (o-SHO) is the kinetic product in the current system as it is a necessary intermediate step to decompose into the equilibrium configuration, which in this system would be SnO, HfO_2, and PbClF. Powder XRD data of the unwashed 0 h, 12 h, 24 h, and 72 h products (Figure S2) demonstrates this with evolution of PbClF up to 24 h, while SnO and HfO_2 begin to form as the perovskite decomposes beyond 24 h of heating. Higher temperatures lead to complete decomposition while lower temperatures produced no PbClF, i.e., no Sn(II)-exchange.

Total energy calculations were used to better understand why two distinct $SnHfO_3$ (SHO) polymorphs can be synthesized using similar conditions and changing the precursor. The results of these data are summarized in Figure 1B,C. The total internal energies of the ideal cubic (c-SHO), the previously synthesized pseudocubic (p-SHO), and currently synthesized o-SHO, were determined to be −8.205, −8.238, and −8.271, respectively, all in eV per formula unit. The relative metastabilities were calculated by the experimentally confirmed decomposition reaction, shown below in eq. 2:

$$SnHfO_3 \rightarrow SnO + HfO_2 \ \Delta E_{decomp} < 0 \quad (2)$$

The results show the c-SHO polymorph is the most metastable at −646 meV atom^{-1}, while the p-SHO model is more stable at −613 meV atom^{-1}, consistent with prior observations. The o-SHO model provides additional stabili-

© 2023 The Authors. Angewandte Chemie International Edition published by Wiley-VCH GmbH

15213773, 0, Downloaded from https://onlinelibrary.wiley.com/doi/10.1002/anie.202312130 by North Carolina State Universit, Wiley Online Library on [18/10/2023]. See the Terms and Conditions (https://onlinelibrary.wiley.com/terms-and-conditions) on Wiley Online Library for rules of use; OA articles are governed by the applicable Creative Commons License

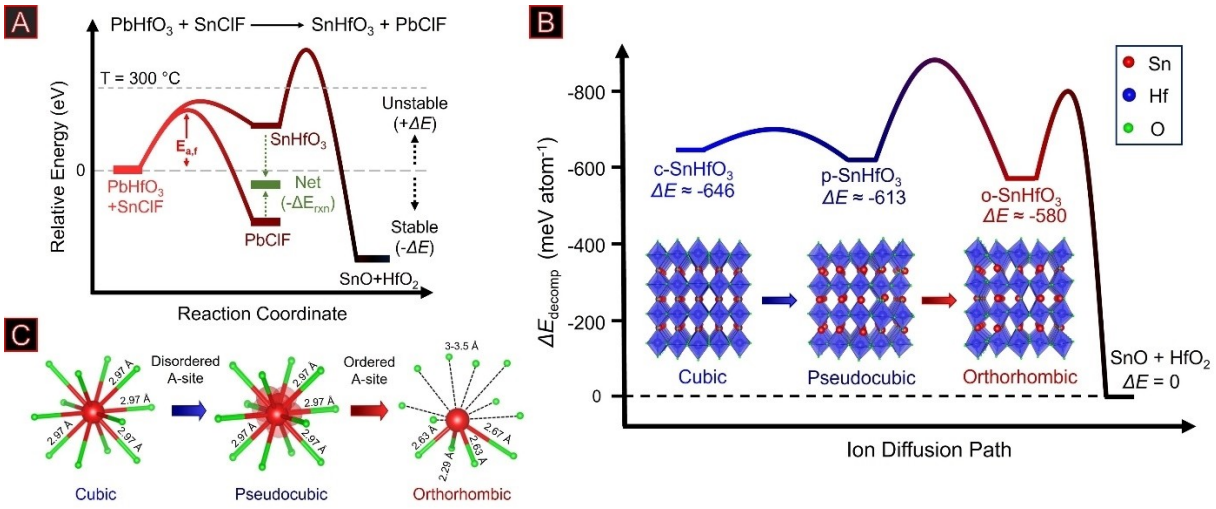

Figure 1. Schematic representation of $SnHfO_3$ synthesis via molten SnClF ion-exchange (A), schematic diagram of ion diffusion pathways from high to low symmetries with an emphasis on HfO_6 substructure tilting (B), and illustration of A-site distortions (C). Orthorhombic $PbHfO_3$ (o-PHO) is reacted with SnClF to form orthorhombic $SnHfO_3$ (o-SHO) and PbClF. In previous work, cubic and pseudocubic $SnHfO_3$ (c-SHO and p-SHO) were synthesized from $BaHfO_3$ at lower temperatures. Octahedral tilting and A-site distortions are each calculated to provide a ~30 meV atom^{-1} stabilizing effect. However, kinetic barriers to structural rearrangement are larger than the next activation barrier that then leads to decomposition to SnO and HfO_2. Local Sn(II)-displacements on the A-site have only small kinetic barriers. Activation energy barriers are estimated by relative decomposition amounts experimentally observed.

zation with a metastability of −580 meV atom^{-1}. The structural models of each polymorph in Figure 1B,C highlight the origin of the stability. The Hf–O substructure largely remains unchanged from the c-SHO to p-SHO transition but allows random A-site distortions, providing a ≈30 meV atom^{-1} calculated stabilization. The HfO_6 polyhedron tilts significantly from p-SHO to o-SHO while the A-site is already asymmetric, providing an additional stabilizing effect. The pseudocubic SHO decomposes thermally upon annealing and does not recrystallize as orthorhombic, indicating a larger kinetic barrier between p-SHO and o-SHO than decomposition.

Combining the kinetic and thermodynamic data, the coordination environments for both Sn(II) and Hf(IV) are at local minima configurations in the perovskite structure for $SnHfO_3$ but are metastable. With sufficient thermal energy, the Sn(II)-cation has no barriers preventing diffusion off the A-site center, as in p-SHO, but is kinetically trapped to prevent formation of SnO. The high lattice energy of the Hf–O substructure inhibits its distortion. It has a large barrier to distort and will decompose to the significantly more stable HfO_2 if enabled, and thus the exchanged product ′remembers′ the precursor structure. The precursor 'memory' effect described above is uncommon but not unknown during the ion exchange of close-packed oxides. For example, the precursor substructures are maintained in the metastable wurtzite $NaGaO_2$ with Cu(I),[29] CdSe nanocrystals with Cu(I) or Zn(II),[30] and rutile $LiNbWO_6$ with Fe(II).[31] In layered phases this is more common as the ions diffuse freely to energetically favorable coordination environments, such as in $K_2Ln_2Ti_3O_{10}$ Ruddlesden-Popper and Dion-Jacobson phases[32] or in potassium titanates such as $K_2Ti_2O_5$.[33]

High resolution XRD data were collected for the o-SHO product. Results of Rietveld refinements from 5–90° 2θ are summarized in Figure 2D and are in good agreement with the *Pbam* space group (no. 55) using the refined PHO precursor as an initial model, with *wRp* of ≈6 % and lattice parameters of $a = 5.8496(3)$, $b = 11.7121(5)$, $c = 8.2163(2)$, all in Å. The lattice parameters have decreased by <0.1 %, similar to previous Sn(II) perovskites.[24,25] The inset shows that some secondary phases of SnO, HfO_2, and PbClF are observed as well. The secondary phases were not modeled in the refinements due to the low resolution and intensities. Two *Pbam* models were used to refine $SnHfO_3$, with alternative perovskite structure-types (i.e., *Pba*2 and *Amm*2) resulting in poorer fittings. The first model set Pb and Sn initial occupancies at 1.0 and 0.0, respectively, and freely refined to give Sn occupancies of 0.83(1) and 0.89(1) on the 4*g* and 4*h* Wyckoff sites, respectively. In the second model, the Sn fraction was set to unity, with no lead, to refine against vacancies. The second model resulted in better low angle peak fitting and increased stability of the refinement, as well as greater consistency with electron microscopy data discussed below. Additional crystallographic information for both the PHO precursor and o-SHO product are summarized in Tables S1–S3 and Figure S3. Two low intensity peaks at ≈7 and ≈9° were also observed that are not modeled. These two low intensity peaks could not be identified but may represent finer-level distortions of the perovskite structure,[34,35] as also probed below. The peak at ≈21° is overestimated by the refinement. Further attempts to improve the fit neither resulted in a chemically relevant nor unique solution except when Hf occupancies decreased to ≈0.95, which is within reason as observed by the presence of HfO_2. More advanced structural characterization techniques

© 2023 The Authors. Angewandte Chemie International Edition published by Wiley-VCH GmbH

15213773, 0, Downloaded from https://onlinelibrary.wiley.com/doi/10.1002/anie.202312130 by North Carolina State Universit, Wiley Online Library on [18/10/2023]. See the Terms and Conditions (https://onlinelibrary.wiley.com/terms-and-conditions) on Wiley Online Library for rules of use; OA articles are governed by the applicable Creative Commons License

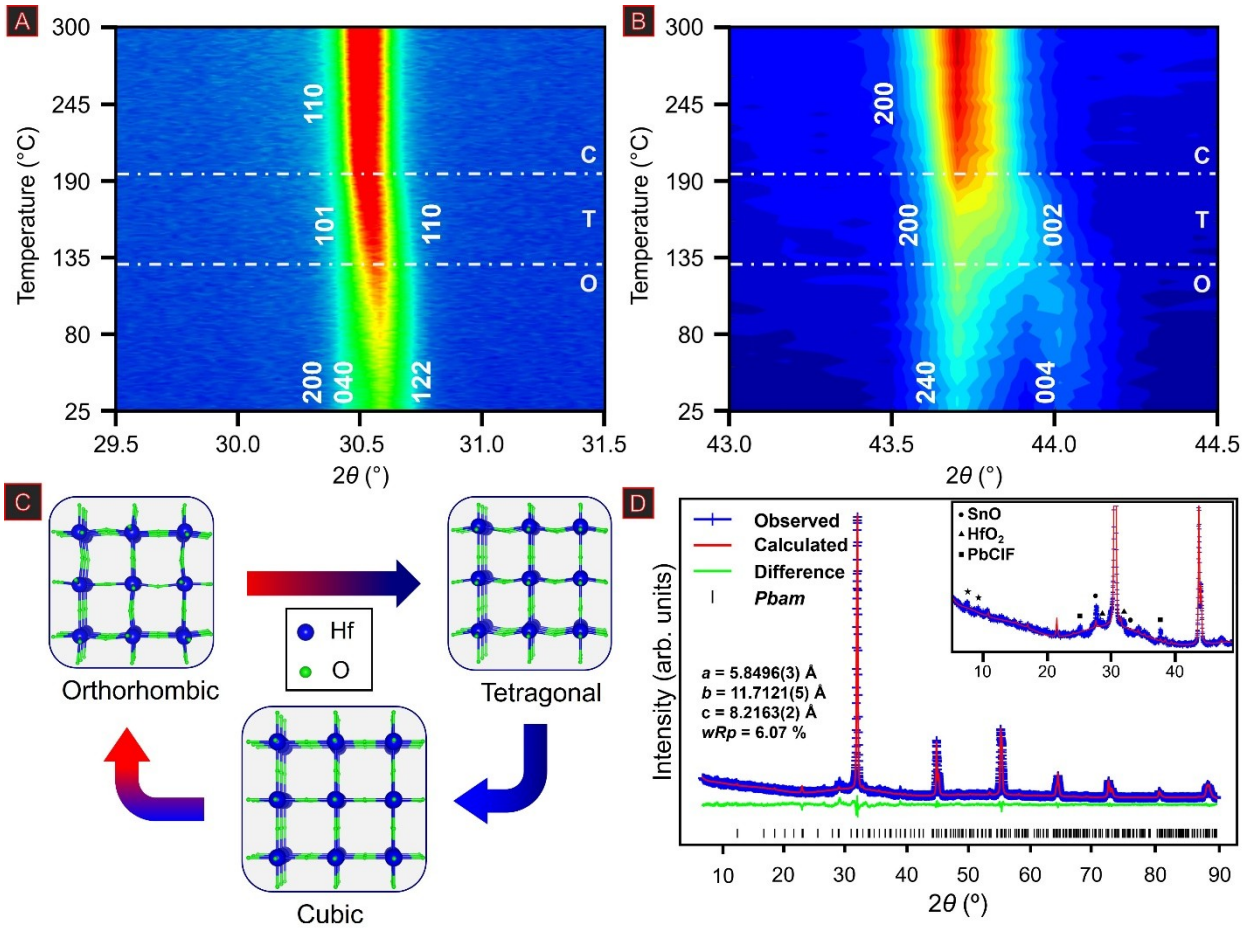

Figure 2. Selected bulk structural characterization data shown as temperature-dependent XRD of $SnHfO_3$ focused on the {110}-family peak (A) and the {200}-family peak (B), schematic representation of Hf–O substructure phase changes (C), and full-profile Rietveld refinement of $SnHfO_3$ at room temperature with space group *Pbam* (D). $SnHfO_3$ undergoes a phase transition from *Pbam* to a higher symmetry phase at ≈130 °C, then to a second phase at ≈200 °C. The phases were assigned based upon previously investigated $PbHfO_3$ phase changes. (D, inset) Secondary phases are marked as ● for SnO, ▲ for HfO_2, ■ for PbClF, and * for the low angle peaks observed in $SnHfO_3$.

than powder XRD are required in future studies to fully reveal the fine structure of o-SHO, such as neutron diffraction.

Temperature-dependent in situ XRD was performed on o-SHO to probe the possible existence of structural phase changes (Figure S4 and S5) and the findings are summarized in Figure 2A–C. During heating from 25–300 °C, the peak at ≈30.5° (2θ) grows significantly in intensity at ≈130 °C and further at ≈200 °C. The doublet of peaks at ≈43.8° (2θ) converge closely at ≈130 °C and into a single peak at ≈200 °C. These transitions can be attributed to both the {110} and {200} family, which are triplets in the orthorhombic setting, converging to two peaks closer in *d*-spacing, or $a \neq b \neq c \rightarrow a = b \neq c$, then once more to a cubic setting, $a = b = c$. At least two phase changes occur to higher perovskite symmetries with Curie temperatures (T_c) of 130 °C and 200 °C. Both transitions were observed to be reversible upon cooling to 25 °C. A graphical representation of the phase transitions are shown in Figure 2C and assigned based upon previous investigation of the PHO fine structure.[36] The structure of PHO undergoes reversible phase changes beginning at 150 °C, then to polar phase at 180 °C, then finally to $Pm\bar{3}m$ at 220 °C. The intermediate structures for PHO are still under active investigation.[37,38] The observed decrease in T_c by ≈20 °C with smaller A-site cation substitution has been observed in other systems such as $BaTiO_3$ and hypothesized in other compositions.[39] Interestingly, the intermediate *C2mm* and *P4mm* PHO phases are polar. The low thermal stability of o-SHO (onset T_{decomp} ≈350 °C, Figure S15) enables further investigation into the potential ferroelectricity at ≈130–200 °C and representing a promising direction for attaining a polar Sn(II)-perovskite oxide.

The PHO precursor and o-SHO polycrystalline powders were probed by scanning electron microscopy (SEM) and Energy Dispersive Spectroscopy (EDS) at low magnification to observe changes after Sn(II)-substitution. Representative images of PHO and o-SHO are shown in Figure S6,S7 with a summary of EDS data shown in Table S4. SEM-EDS demonstrates the PHO precursor is consistent with the expected Pb:Hf stoichiometry of close to ≈1:1 and elemental mappings showing the homogeneity and high-

© 2023 The Authors. Angewandte Chemie International Edition published by Wiley-VCH GmbH

15213773, 0, Downloaded from https://onlinelibrary.wiley.com/doi/10.1002/anie.202312130 by North Carolina State University, Wiley Online Library on [18/10/2023]. See the Terms and Conditions (https://onlinelibrary.wiley.com/terms-and-conditions) on Wiley Online Library for rules of use; OA articles are governed by the applicable Creative Commons License

purity of the precursor phase. When SnClF was loaded at a nominal 25 % substitution, the Sn:Hf ratio became ≈1/3 and the Pb decreased to ≈2/3. At 50 % SnClF loading, the Pb:Sn:Hf ratio was ≈1:1:2, and consistent with half Sn substitution. The PbClF salt is alsoin large enough concentration to detect Cl and F. After 100 % loading of SnClF, Sn is now detected in a large amount in a ≈1:1 ratio with Hf. Pb is still present in an appreciable amount, albeit significantly decreased. Elemental mapping shows the remaining Pb concentrated as crystallites where Sn and Hf are depleted, and the Pb:Cl+F ratio is ≈1:2. The SEM-EDS strongly supports either a high degree or complete Sn-substitution in particles and that the primary source of remaining Pb is the poorly soluble salt.

The $SnHfO_3$ product was further investigated by scanning transmission electron microscopy (STEM) for characterization of representative particles and to avoid Pb-salt impurities in elemental composition determinations. Figure 3 shows a representative particle with elemental mapping and EDS spectra (additional images in Figure S8–10) in addition to the ^{119}Sn Mössbauer spectrum. The EDS spectra (Figure S8) show Sn, Hf, O, along with Cu and C, attributed to the copper grid and carbon support film. A small amount of Pb was detected but none in the particle according to the elemental mapping. EDS line-scans show the particle composition of Sn:Hf:O is ≈1:1:3 throughout the particle and consistent with the perovskite stoichiometry ABO_3. There is some larger variation of Sn and Hf outside of standard EDS error margins, which is attributed to SnO_2 from surface oxidation. Pb was detected at <0–5 mol% and Cl at ≈5 mol%. The Pb is well within EDS error for background level. The Cl is somewhat larger which could be from incorporation into the perovskite, surface corrosion from the halide flux, or the residual lead salt.

The ^{119}Sn Mössbauer spectrum of $SnHfO_3$ is presented in Figure 3B and the fitting parameters are summarized in Table S5. The spectrum is well reproduced with three sub-signals, two of them show the presence of Sn(II) and the third sub-signal is in the typical range of Sn(IV).[40] The observed isomer shift (3.06 mm s^{-1}) of the majority fraction can be attributed to Sn(II) atoms on the A-site of perovskite-type $SnHfO_3$. The experimental line width is slightly enhanced. Due to possible substitution of Hf by Sn,[41] varying coordination environments for the Sn(II) cations could co-exist. Therefore, the simulated signal envelopes sub-signals, which corresponds to different Sn(II) environments. The large quadrupole splitting (2.00 mm s^{-1}) indicates distortion of the cuboctahedral coordination of the Sn(II) ions because of its stereoactive lone pair. Similar environments for Sn(II) are reported for BSZT and ilmenite-type $SnTiO_3$ with isomer shifts of around 3 mm s^{-1} and quadrupole splittings of about 1.8 mm s^{-1} and 1.45 mm s^{-1}.[42] The isomer shift (−0.03 mm s^{-1}) and quadrupole splitting (0.6 mm s^{-1}) of the minority Sn(IV) fraction (10 %) match Mössbauer spectroscopic data observed for (nano−)SnO_2 and can be attributed to surface oxidation of Sn(II),[43,44] similar to observations described for BSZT and $SnTiO_3$.[45,46] In the typical range of Sn(II)-compounds there is an additional signal (9 %). The observed Mössbauer spectroscopic data (δ=4.2 mm s^{-1}, ΔE_Q=0 mm s^{-1}) agrees with previously reported data for $SnCl_2$ (4.06 mm s^{-1}, 0 mm s^{-1}).[47,48]

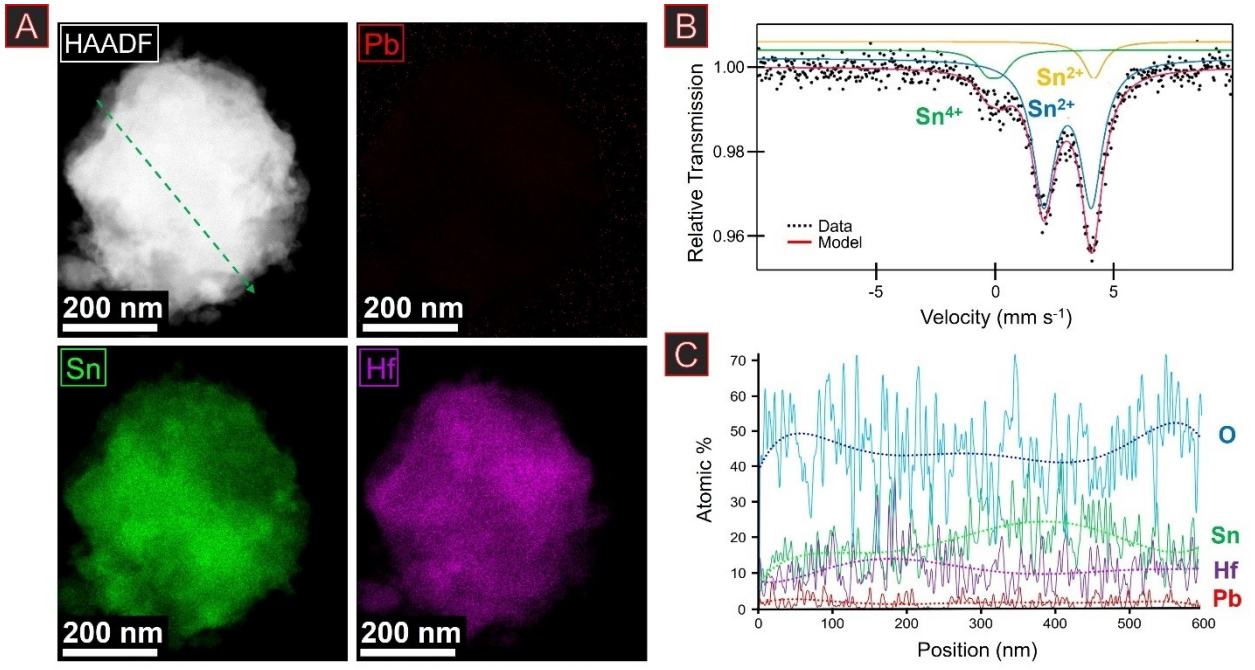

Figure 3. STEM/EDS images and elemental maps of Pb, Sn, and Hf of a representative particle (A), Experimental (data points) and simulated (colored lines) ^{119}Sn Mössbauer spectrum of $SnHfO_3$ measured at 78 K (B), and EDS line scan (C) of $SnHfO_3$. For EDS results, Sn is shown in green, Hf in purple, O in blue, and Pb in red. The green line shown in (A) depicts the line scan path. Dotted EDS lines are moving averages added for visual clarity. Simulated Mössbauer data are shown as Sn(II) in blue for $SnHfO_3$, Sn(II) in yellow for SnClF, and Sn(IV) for SnO_2 in green.

© 2023 The Authors. Angewandte Chemie International Edition published by Wiley-VCH GmbH

15213773, 0, Downloaded from https://onlinelibrary.wiley.com/doi/10.1002/anie.202312130 by North Carolina State Universit, Wiley Online Library on [18/10/2023]. See the Terms and Conditions (https://onlinelibrary.wiley.com/terms-and-conditions) on Wiley Online Library for rules of use; OA articles are governed by the applicable Creative Commons License

Selected area electron diffraction (SAED) was used to further investigate the $SnHfO_3$ nanostructure. However, most particles showed polycrystalline or amorphous diffraction (Figure S11). One representative sample produced an ED pattern, shown in Figure 4A. The indexable reflections in the diffraction pattern are in agreement with the *Pbam* space group projected down the [111] zone axis. The indexed planes are the {110} type reflections with a *d*-spacing of ≈11.7 Å and the {211} type with *d*-spacing of ≈6.67 Å. The polycrystalline nature prevents more detailed investigation into the fine structure such as octahedral tilting, which would be observable via ED techniques.[49] Figure 4B shows near-atomic resolution of the same particle surface, in which lattice spacing is visible on the particle surface. Real-space distances of ≈11.17 Å between the planes are consistent with the 110 spacing observed in the XRD refinement. There is also an amorphous shell around the particle edge, which stems from the surface oxidized SnO_2. The STEM data conclusively shows that the $SnHfO_3$ product is fully Sn-substituted and retains the long range structure generally consistent with the *Pbam* space group.

Total Densities-of-States (DOS) and electron density calculations were performed to probe the changes in electronic structure upon going from $PbHfO_3$ (PHO) to the new orthorhombic $SnHfO_3$ (o-SHO) perovskite. The prototypical cubic ABO_3 perovskite has a valence band (VB) comprised of primarily filled O $2p^6$ orbitals and conduction band (CB) consisting of the B-metal nd^0 orbitals. In the case of PHO (Figure S12), the VB is predominantly O $2p^6$. However, the CB is now comprised of unfilled Pb-6*p* states mixed with O-2*p* states, with the empty Hf 5*d* states higher in energy. The relatively shorter Pb–O distances arise from the asymmetric distortion of Pb(II) and its stereoactive lone pair, thus distorting it toward neighboring O. Its band gap predicted from DOS calculations is a relatively smaller value of ≈3.0 eV as compared to the experimental value of ≈3.6 eV (Figure S13). This underestimation of the band gap by DFT methods is well documented.[50] For the new o-SHO, by comparison, the results of DOS calculations and projected electron densities at the valence and conduction band edges are shown in Figure 5. These plots show the calculated VB for o-SHO is still comprised predominantly of filled O-2*p* (blue curve) and with contributions from Sn-5*s* states (green curve). Contributions of the Sn-5*s* states at the VB edge are larger as compared to the Pb-6*s* states at the VB edge for PHO. This results from the relatively higher energy Sn-5*s* orbitals that are closer in energy to the O 2*p* states and mix to a greater extent, as described previously for main group oxides and perovskites,[17,24,25] and thus raising the energy of the VB edge. Conversely, the CB edge is composed of predominantly empty Sn-5*p* states at lower energies and mixed with a smaller contribution from O-2*p* states. Given the replacement of the Pb(II) with the isoelectronic Sn(II) cation, the A-site distortion also leads to an asymmetric electron density that is consistent with a lone pair. The smaller calculated band gap for o-SHO of ≈2.2 eV stems from these changes in electronic structure and is consistent with the redshifted experimental value of ≈2.6 eV (Figure S13). The lower-symmetry structure of o-SHO results in a smaller band gap as compared also to pseudo-cubic $SnHfO_3$ (p-SHO) of ≈3.7 eV. This trend suggests the A-site distortion of the Sn(II) cation leads to a raising of the energy of the VB edge most predominantly.

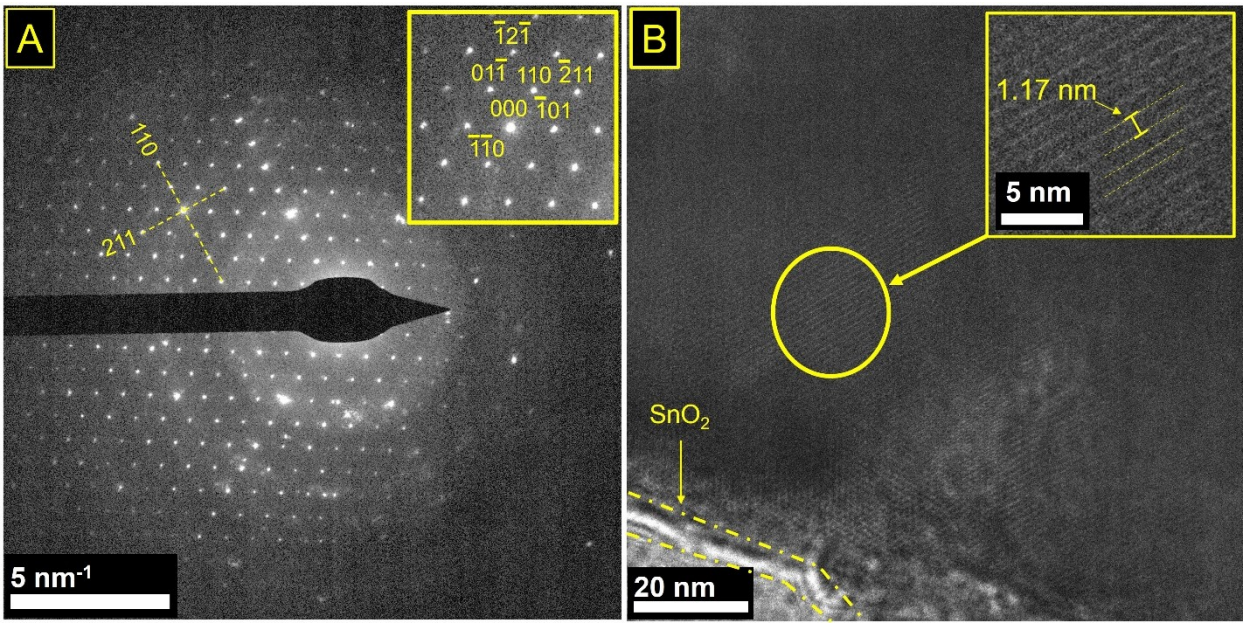

Figure 4. Selected area electron diffraction (A) and scanning transmission electron microscope image (B) of a $SnHfO_3$ crystal. The ED beam is projected down the [111] axis revealing the {110} family (d ≈11.7 Å) and the {211} family (d ≈6.67 Å). Planes observed on the particle surface have a spacing of ~11.7 Å corresponding to (110)-type stacking. A thin shell of amorphous SnO_2 is visible on the particle surface owing to surface oxidation of Sn(II).

© 2023 The Authors. Angewandte Chemie International Edition published by Wiley-VCH GmbH

15213773, 0, Downloaded from https://onlinelibrary.wiley.com/doi/10.1002/anie.202312130 by North Carolina State University, Wiley Online Library on [18/10/2023]. See the Terms and Conditions (https://onlinelibrary.wiley.com/terms-and-conditions) on Wiley Online Library for rules of use; OA articles are governed by the applicable Creative Commons License

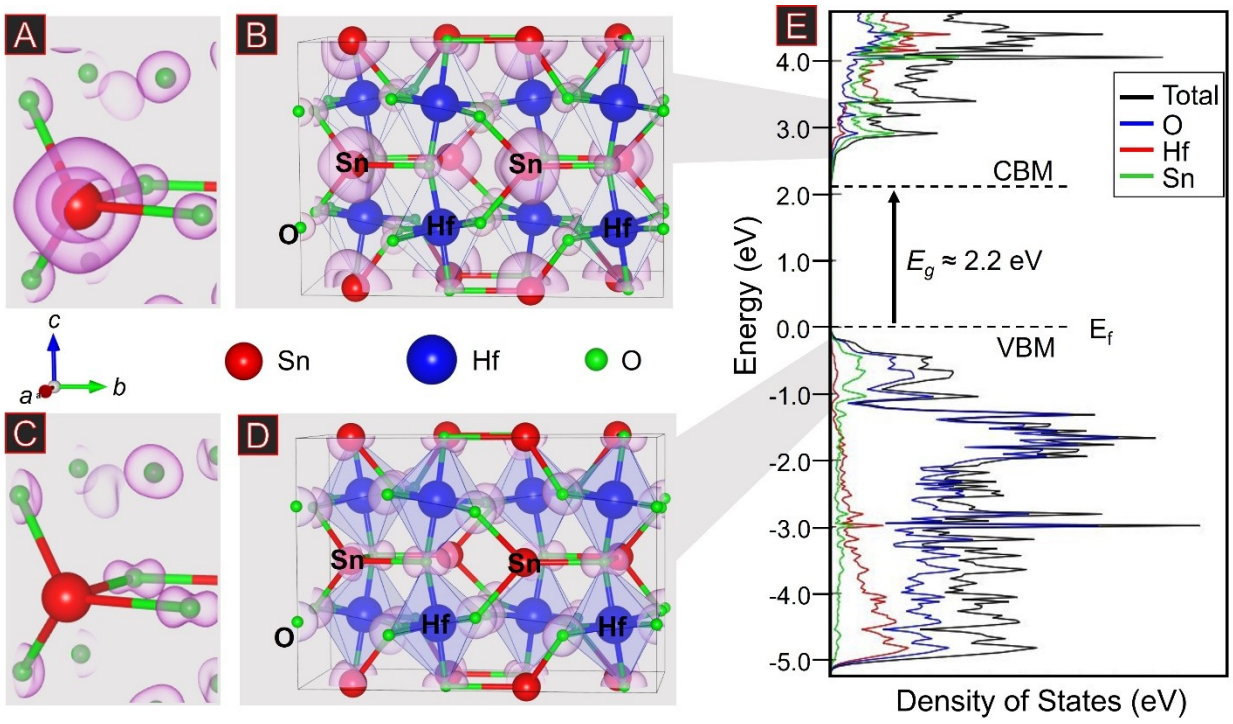

Figure 5. Calculated electron density maps for the conduction band edge (A,B) and valence band edge (C,D) along with the total densities-of-states (E) for the $SnHfO_3$ perovskite in space group *Pbam*. Emphasis around the Sn–O local coordination is shown in A and C for clarity, with the unit cells shown in B and D. Projected electron density is localized around O in the valence band edge and around Sn and O in the conduction band. The calculated band gap is ≈2.2 eV. Electron density projections are displayed in pink and atoms are shown as Sn in red, Hf in blue, and O in green.

The Born effective charge (BEC; Z*) tensor quantities for the ions in o-SHO were calculated using density functional perturbation theory methods and a 2×1×2 supercell, as detailed in the Supporting Information. The BECs are a measure of the resulting change in macroscopic polarization induced by ion displacements and, for ferroic materials, are typically larger than the nominal oxidation states.[51] Table S6 lists the BEC tensors for each ion in the *Pbam* space group, with maximal diagonal values for the tensors of Hf (+5.86), Sn1 (+3.69;), Sn2 (+3.60) and for all O atoms (−3.641 to −2.671). These relatively large values compare reasonably well to those in antiferroelectric hafnate and zirconate perovskites,[51,52] such as for $PbZrO_3$ with BECs for Pb (+3.89) and for Zr (+5.90). Notably, the ground-state structures of antiferroelectric $PbHfO_3$ as well as $PbZrO_3$, the archetypical antiferroelectric, have received recent attention and re-examination. Recent studies have unveiled the dynamic instabilities in their phonon band structures and leading to the proposal of new 80-atom, i.e., doubled, superstructures that have yet to be experimentally confirmed.[52,53] Given the isoelectronic nature of Sn(II) and Pb(II) cations, the calculated phonon band structure of $SnHfO_3$ in space group *Pbam*, shown in Figure S14, is also found to exhibit dynamic instability in the vicinity of the Z and T *q*-points. This observation is also consistent with its metastable nature, and thus requiring kinetic stabilization. These dynamical instabilities at q-points away from the zone center indicate the likelihood of energetically competitive and fine atomic distortions occurring over longer length scales. Possible superstructure models are under further investigation using Bayesian approaches and neutron diffraction data.

Conclusion

For the first time, a distorted Sn(II)-perovskite oxide, orthorhombic $SnHfO_3$, has been synthesized in high purity and crystallinity by a low temperature ion-exchange technique. These results demonstrate the complete removal of Pb from the orthorhombic $PbHfO_3$ perovskite precursor while largely maintaining the sensitive Sn(II) oxidation state as confirmed by XRD, electron microscopy, and ^{119}Sn Mössbauer spectroscopy. Thermodynamic and kinetic considerations of the synthetic approach expand upon our previously proposed mechanism for Sn(II)-exchange of perovskite oxides. Current evidence indicates that the initial ion-exchange step (i.e., Ba(II)/Pb(II) to Sn(II)) does not need to be highly exothermic, but rather the exchange product must be a necessary intermediate step towards the global minimum. Furthermore, these and previous results indicate that ion-exchange techniques at mild conditions allow for much finer structural control of the desired product than previously considered. There are still remaining challenges, such as improving crystallinity or growing single-crystals, fine structural elucidation through advanced diffraction techni-

© 2023 The Authors. Angewandte Chemie International Edition published by Wiley-VCH GmbH

15213773, 0, Downloaded from https://onlinelibrary.wiley.com/doi/10.1002/anie.202312130 by North Carolina State University, Wiley Online Library on [18/10/2023]. See the Terms and Conditions (https://onlinelibrary.wiley.com/terms-and-conditions) on Wiley Online Library for rules of use; OA articles are governed by the applicable Creative Commons License

ques, and improving separation of the Pb-halide salt products. Additionally, in situ XRD suggests the existence of a polar $SnHfO_3$ phase that is stable in the temperature range of 130–200 °C, which requires further exploration. The investigation of $SnHfO_3$ as a model perovskite has allowed deeper insight into the synthetic dynamics of the largely unexplored complex Sn(II)–M–O phase diagram. The successful 'de-leadification' of $PbHfO_3$ has demonstrated that the synthesis of lead-free, isoelectronic, Sn(II) perovskite oxides can be achieved.

Acknowledgements

The authors acknowledge support of this work by the National Science Foundation (DMR-2004455). Additional components of this research were performed in part at the Analytical Instrumentation Facility (AIF) at North Carolina State University, which is supported by the State of North Carolina and the National Science Foundation (Award ECCS-2025064). The AIF is a member of the North Carolina Research Triangle Nanotechnology Network (RTNN), a site in the National Nanotechnology Coordinated Infrastructure (NNCI).

Conflict of Interest

There are no conflicts to declare.

Data Availability Statement

The data that support the findings of this study are available from the corresponding author upon reasonable request.

Keywords: Ion Exchange · Metastable Compounds · Perovskite Phases

[1] S. Lany, *J. Phys.: Condens. Matter* **2015**, *27*, 283203.
[2] G. Trimarchi, X. Zhang, A. J. Freeman, A. Zunger, *Phys. Rev. B* **2014**, *90*, 161111.
[3] V. A. Ha, F. Ricci, G. M. Rignanese, G. Hautier, *J. Mater. Chem. C* **2017**, *5*, 5772–5779.
[4] P. A. Maggard, *Acc. Chem. Res.* **2021**, *54*, 3160–3171.
[5] C. M. Caskey, R. M. Richards, D. S. Ginley, A. Zakutayev, *Mater. Horiz.* **2014**, *1*, 424–430.
[6] A. Zakutayev, A. J. Allen, X. Zhang, J. Vidal, Z. Cui, S. Lany, M. Yang, F. J. DiSalvo, D. S. Ginley, *Chem. Mater.* **2014**, *26*, 4970–4977.
[7] D. B. Straus, S. Guo, R. J. Cava, *J. Am. Chem. Soc.* **2019**, *141*, 11435–11439.
[8] M. Aykol, S. S. Dwaraknath, W. Sun, K. A. Persson, *Sci. Adv.* **2018**, *4*, eaaq0148.
[9] J. Gopalakrishnan, *Chem. Mater.* **1995**, *7*, 1265–1275.
[10] S. K. Gupta, Y. A. Mao, *Prog. Mater. Sci.* **2021**, *117*, 100734.
[11] M. S. Whittingham, *Curr. Opin. Solid State Mater. Sci.* **1996**, *1*, 227–232.
[12] W. A. England, J. B. Goodenough, P. J. Wiseman, *J. Solid State Chem.* **1983**, *49*, 289–299.
[13] E. Gabilondo, S. O'Donnell, R. Newell, R. Broughton, M. Mateus, J. L. Jones, P. A. Maggard, *Chem. Eur. J.* **2022**, *28*, e202200479.
[14] A. J. Bell, O. Deubzer, *MRS Bull.* **2018**, *43*, 581–587.
[15] R. E. Cohen, *Nature* **1992**, *358*, 136–138.
[16] A. K. Tagantsev, K. Vaideeswaran, S. B. Vakhrushev, A. V. Filimonov, R. B. Burkovsky, A. Shaganov, D. Andronikova, A. Rudskoy, A. Q. R. Baron, H. Uchiyama, D. Chernyshov, A. Bosak, Z. Ujma, K. Roleder, A. Majchrowski, J.-H. Ko, N. Setter, *Nature* **2013**, *4*, 2229.
[17] A. Walsh, D. J. Payne, R. G. Egdell, G. W. Watson, *Chem. Soc. Rev.* **2011**, *40*, 4455–4463.
[18] M. F. M. Taib, M. K. Yaakob, O. H. Hassan, M. Z. A. Yahya, *Integr. Ferroelectr.* **2013**, *142*, 119–127.
[19] J. Gardner, A. Thakre, A. Kumar, J. F. Scott, *Rep. Prog. Phys.* **2019**, *82*, 092501.
[20] C. M. Campo, J. E. Rodríguez, A. E. Ramírez, *Heliyon* **2016**, *2*, e00112.
[21] N. Kumada, Y. Yonesaki, T. Takei, N. Kinomura, S. Wada, *Mater. Res. Bull.* **2009**, *44*, 1298–1300.
[22] S. O'Donnell, A. Hamilton, P. A. Maggard, *J. Electrochem. Soc.* **2019**, *166*, H3084–H3090.
[23] L. Diehl, S. Bette, F. Pielnhofer, S. Betzler, I. Moudrakovski, G. A. Ozin, R. Dinnebier, B. V. Lotsch, *Chem. Mater.* **2018**, *30*, 8932–8938.
[24] S. O'Donnell, C. C. Chung, A. Carbone, R. Broughton, J. L. Jones, P. A. Maggard, *Chem. Mater.* **2020**, *32*, 3054–3064.
[25] E. A. Gabilondo, S. O'Donnell, R. Broughton, J. L. Jones, P. A. Maggard, *J. Solid State Chem.* **2021**, *302*, 122419.
[26] S. O'Donnell, A. Smith, A. Carbone, P. A. Maggard, *Inorg. Chem.* **2022**, *61*, 4062–4070.
[27] S. O'Donnell, D. J. Osborn, G. Krishnan, T. Block, A. Koldemir, T. D. Small, R. Broughton, J. L. Jones, R. Pöttgen, G. G. Andersson, G. F. Metha, P. A. Maggard, *Chem. Mater.* **2022**, *34*, 8054–8064.
[28] E. A. Gabilondo, R. J. Newell, J. Chestnut, J. Weng, J. L. Jones, P. A. Maggard, *Nanoscale Adv.* **2022**, *4*, 5320–5329.
[29] H. Nagatani, I. Suzuki, M. Kita, M. Tanaka, Y. Katsuya, O. Sakata, S. Miyoshi, S. Yamaguchi, T. Omata, *Inorg. Chem.* **2015**, *54*, 1698–1704.
[30] H. Li, M. Zanella, A. Genovese, M. Povia, A. Falqui, C. Giannini, L. Manna, *Nano Lett.* **2011**, *11*, 4964–4970.
[31] V. Meena, T. K. Mandal, *Inorg. Chem.* **2019**, *58*, 2921–2924.
[32] R. E. Schaak, T. E. Mallouk, *J. Am. Chem. Soc.* **2000**, *122*, 2798–2803.
[33] Y. Hosogi, H. Kato, A. Kudo, *J. Phys. Chem. C* **2008**, *112*, 17678–17682.
[34] C. M. Handley, R. E. Ward, C. L. Freeman, I. M. Reaney, D. C. Sinclair, J. H. Harding, *Acta Crystallogr. Sect. A* **2023**, *79*, 163–170.
[35] A. M. Glazer, *Acta Crystallogr.* **1972**, *B28*, 3384–3392.
[36] M. F. Kupriyanov, E. V. Petrovich, E. V. Dutova, Y. V. Kabirov, *Crystallogr. Rev.* **2012**, *57*, 205–207.
[37] A. Bosak, V. Svitlyk, A. Arakcheeva, R. Burkovsky, V. Diadkin, K. Roleder, D. Chernyshov, *Acta Crystallogr. Sect. B* **2020**, *76*, 7–12.
[38] R. G. Burkovsky, I. Bronwald, D. Andronikova, G. Lityagin, J. Piecha, S.-M. Souliou, A. Majchrowski, A. Filimonov, A. Rudskoy, K. Roleder, A. Bosak, A. Tagantsev, *Phys. Rev. B* **2019**, *100*, 014107.
[39] J. Ravez, *C. R. Acad. Sci. II C* **2000**, *3*, 267–283.
[40] G. K. Shenoy, F. E. Wagner, *Mössbauer Isomer Shifts*, North-Holland Publishing Company, Amsterdam, NL, **1978**.
[41] R. Mackay, A. W. Sleight, M. A. Subramanian, *J. Solid State Chem.* **1996**, *121*, 437–442.

© 2023 The Authors. Angewandte Chemie International Edition published by Wiley-VCH GmbH

15213773, 0, Downloaded from https://onlinelibrary.wiley.com/doi/10.1002/anie.202312130 by North Carolina State Universit, Wiley Online Library on [18/10/2023]. See the Terms and Conditions (https://onlinelibrary.wiley.com/terms-and-conditions) on Wiley Online Library for rules of use; OA articles are governed by the applicable Creative Commons License

[42] L. Diehl, D. H. Fabini, N. Vargas-Barbosa, A. Jiménez-Solano, T. Block, V. Duppel, I. Moudrakovski, K. Küster, R. Pöttgen, B. V. Lotsch, *Chem. Mater.* **2021**, *33*, 2824–2836.
[43] A. de Kergommeaux, J. Faure-Vincent, A. Pron, R. de Bettignies, B. Malaman, P. Reiss, *J. Am. Chem. Soc.* **2012**, *134*, 11659–11666.
[44] G. S. Collins, T. Kachnowski, N. Benczer-Koller, *Phys. Rev. B* **1979**, *19*, 1369–1373.
[45] S. Indris, M. Scheuermann, S. M. Becker, V. Šepelák, R. Kruk, J. Suffner, F. Gyger, C. Feldmann, A. S. Ulrich, H. Hahn, *J. Phys. Chem. C* **2011**, *115*, 6433–6437.
[46] Y. S. Avadhut, J. Weber, E. Hammarberg, C. Feldmann, I. Schellenberg, R. Pöttgen, J. S. Günne, *Chem. Mater.* **2011**, *23*, 1526–1538.
[47] J. D. Donaldson, B. J. Senior, *J. Chem. Soc. A* **1969**, 2358–2360.
[48] N. N. Greenwood, A. Timnick, *J. Chem. Soc. A* **1971**, 676–678.
[49] D. I. Woodward, I. M. Reaney, *Acta Crystallogr.* **2005**, *B61*, 387–399.
[50] J. P. Perdew, *Int. J. Quantum Chem.* **1985**, *28*, 497–523.
[51] L. Xie, J. Zhu, *J. Am. Ceram. Soc.* **2012**, *95*, 3597–3604.
[52] H. Aramberri, C. Cazoria, M. Stengei, J. Iniguez, *npj Comput. Mater.* **2021**, *7*, 196.
[53] J. S. Baker, *Long Range Order in Ferroelectric and Antiferroelectric Perovskites Meets Large Scale Density Functional Theory*. Doctoral dissertation, London Center for Nanotechnology, **2020**.

Manuscript received: August 18, 2023
Accepted manuscript online: September 12, 2023
Version of record online: ■■, ■■

© 2023 The Authors. Angewandte Chemie International Edition published by Wiley-VCH GmbH

15213773, 0, Downloaded from https://onlinelibrary.wiley.com/doi/10.1002/anie.202312130 by North Carolina State Universit, Wiley Online Library on [18/10/2023]. See the Terms and Conditions (https://onlinelibrary.wiley.com/terms-and-conditions) on Wiley Online Library for rules of use; OA articles are governed by the applicable Creative Commons License

Research Articles

Perovskite Phases

E. A. Gabilondo, R. J. Newell, R. Broughton, A. Koldemir, R. Pöttgen, J. L. Jones, P. A. Maggard* ——— **e202312130**

Switching Lead for Tin in $PbHfO_3$: Non-cubic Structure of $SnHfO_3$

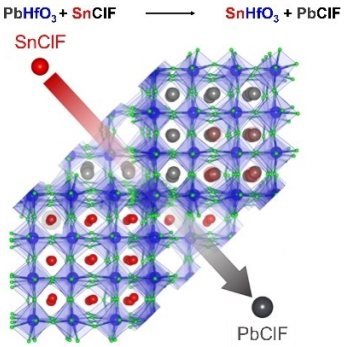

The replacement of Pb(II) for Sn(II) cations in perovskite oxides is challenging because of their high thermodynamic instability. A new orthorhombic $SnHfO_3$ perovskite has been synthesized via removal of Pb(II) cations from $PbHfO_3$ by reaction with a SnClF salt.

© 2023 The Authors. Angewandte Chemie International Edition published by Wiley-VCH GmbH

15213773, 0, Downloaded from https://onlinelibrary.wiley.com/doi/10.1002/anie.202312130 by North Carolina State Universit, Wiley Online Library on [18/10/2023]. See the Terms and Conditions (https://onlinelibrary.wiley.com/terms-and-conditions) on Wiley Online Library for rules of use; OA articles are governed by the applicable Creative Commons License